Multifunctional Silver-Enzyme Nanogels Assembly with Efficient Trienzyme Cascades for Synergistic Diabetic Wound Healing

Yedong Ma, Xiyu Lai, Xi Luo, Zheng Luo, Liuzhou Mao, Houjuan Zhu, Xiaotong Fan, Junhua Kong, Yun-Long Wu*, Zibiao Li*, Chaobin He**

Y. Ma, Z. Li, C. He**
Department of Materials Science and Engineering, National University of Singapore, 9 Engineering Drive 1, Singapore 117576, Singapore
Email: msehc@nus.edu.sg

*X. Lai, Z. Luo, L. Mao, Y. Wu**
Fujian Provincial Key Laboratory of Innovative Drug Target Research and State Key Laboratory of Cellular Stress Biology, School of Pharmaceutical Sciences, Xiamen University, Xiamen, China
Email: wuyl@xmu.edu.cn

X. Luo
Drug clinical trial institution, The first affiliated hospital of Xiamen University, Xiamen, Fujian, China

X. Fan, Z. Li**
*Institute of Sustainability for Chemicals, Energy and Environment (ISCE2), Agency for Science, Technology and Research (A*STAR), 1 Pesek Road, Jurong Island, Singapore 627833, Singapore.*
Email: xiaotong_fan@isce2.a-star.edu.sg

H. Zhu, J. Kong, Z. Li, C. He**
*Institute of Materials Research and Engineering (IMRE), Agency for Science, Technology, and Research (A*STAR), 2 Fusionopolis Way, Innovis, Singapore 138634, Singapore*
Email: lizb@imre.a-star.edu.sg

Keywords: diabetic wound healing, enzyme nanogel, assembly, enzymatic cascade reaction

Abstract

Diabetic wound healing presents a persistent clinical challenge, often characterized by prolonged healing times, and can be particularly difficult to achieve in a hyperglycemic environment. In this study, we design a multi-functional silver-enzyme nanogels assembly (Ag-nGHC) by focusing on the complex diabetic wound environment. Glucose oxidase (GOX), horseradish peroxidase (HRP), and catalase (CAT) are modified within polymeric nanogel layers and assembled into a large enzyme cluster with silver ions. The close attachment of three enzymes ensures fast and continuous consumption of a high level of glucose, generation of oxygen and hydroxyl radicals (•OH) around the wound site. Meanwhile, the silver ions within the Ag-nGHC assembly act as an effective agent to kill bacteria. This cascade enzyme system significantly improve the microenvironment of the wound site by reducing bacterium infection and alleviating hypoxia as well as hyperglycemia. Sequentially, the improved environment facilitates the later processes including anti-inflammatory, re-epithelialization, and angiogenesis, evidenced by enhancing polarization towards M2 macrophages and increasing CD31 signals in our studies. Overall, our Ag-nGHC materials have been proven to achieve multifunctional properties towards complicated diabetic wound healing processes (attributes as adaptability, hypoxia-alleviated, anti-hyperglycemic, antimicrobial, anti-inflammatory, and angiogenic) and showed great potential for the treatment of chronic diabetic wound.

1. Introduction

Diabetes mellitus, recognized globally for its high prevalence, often leads to the development of diabetes foot ulcers (DFU) in patients during its later stages. The occurrence and progression of DFU are not only intricately linked with profound morbidity and mortality rates, evidenced by over 70,000 lower-extremity amputations and a marked decline in the quality of life for affected individuals.[1,2] Distinct from normal acute wounds, the healing process in diabetic wounds is notably impeded by a constellation of factors: hyperglycemia, persistent vascular damage, the dysregulation of inflammatory responses, significant bacterial invasions, tissue hypoxia, and hindered tissue remodeling. Among these, a high level of glucose accumulation at the diabetic wound site is one of the core factors that impede the healing process by reducing blood flow, impairing the function of immune cells like neutrophils and macrophages as well as impeding angiogenesis.[3–5] Glucose oxidase (GOX) appears as a powerful enzyme biocatalyst to consume excess glucose within the hyperglycemic environment due to its effective catalytic activity and substrate specificity towards glucose oxidization.[6,7] GOX is capable of quickly oxidizing glucose into gluconic acid in the presence of oxygen, and meanwhile producing H_2O_2. This reaction can effectively regulate the blood glucose level, facilitating a balanced inflammatory response, immune cell recruitment, and fast wound healing.[8–10] Thus, many strategies have been developed to apply GOX as a therapeutic agent to enhance the hyperglycemic environment.[10,11] However, single GOX alone is not efficient enough to tackle complicated wound environments.

Traditional treatments for chronic wounds, such as nanodrug and dressings, offer limited benefits and fail to address the complex requirements of healing diabetic wounds. Adjusting the microenvironment of diabetic wounds to suit the various phases of healing is crucial for effective treatment.[12–14] To amplify the therapeutic effect of GOX, multi-enzyme cascade reactions involved synergistic actions that work in concert were developed to facilitate various stages of wound healing.[9,14] Complex pathogenesis leads to the occurrence of persistent infections such as vasculopathy and immunopathy. H_2O_2, generated from glucose oxidation catalyzed by GOX, can be further converted into toxic reactive oxidative species (ROS), such as hydroxyl radicals (•OH) by horseradish peroxidase (HRP).[9,16,17] This cascade process is effective at attacking bacterial membranes in the mildly acidic environment of infected wounds.[17] However, the cascade reaction between GOX and HRP in anti-bacterial process is usually restricted by the hypoxia environment and high oxidative stress. Meanwhile, the

toxicity of this cascade reaction poses another threat to normal cell viability, which may harm the anti-inflammation and proliferation healing processes. Catalase (CAT) could catalyze the H_2O_2 degradation to generate H_2O and molecular oxygen, endowing it as an antioxidant to scavenge free radicals that relieve cells from oxidative damage. Moreover, this reaction facilitates to replenish oxygen and alleviate hypoxia.[18–20] Modulating the imbalanced microenvironment of the wound site greatly facilitates critical phases of the later healing process, including cell migration, tissue remodeling, and skin reconstruction.[21,22] Several studies have utilized nanozymes that mimic peroxidase, glucose oxidase, catalase, and superoxide dismutase in diabetic wound healing. [21,23–26] Nevertheless, the limited catalytic efficiency of these nanozymes has constrained their broader application. In contrast, native enzymes exhibit high specificity and catalytic efficiencies, which make them advantageous. Additionally, native enzymes are inherently biocompatible, as they are proteins naturally existing in biological systems.[6,27] They generally exhibit low immunogenicity and cytotoxicity, rendering them suitable for therapeutic applications. However, the fragile nature of native enzymes leads to their rapid degradation under the complex microenvironments of diabetic wounds. Therefore, it is imperative to design appropriate delivery platforms to enhance the stability of these enzymes.

Previous studies have explored various delivery platforms for enzymes, including inorganic particles,[28] metal-organic framework (MOF),[29] liposomes,[30,31] and cationic polymers. [32,33] Single enzyme nanogel (SEN) represents an emerging technology where each enzyme molecule is encapsulated within a thin hydrogel coating.[34,35] This synthesis occurs directly around the enzyme surface, creating structures akin to the core-shell model where the surrounding polymer acts as a safeguarding shell.[36,37] Such configurations typically facilitate to maintain catalytic efficiency comparable to the natural enzymes. These nanogels demonstrate notably improved stability when exposed to high temperatures and in the presence of organic solvents.[38] Additionally, various chemical groups can be modified within the gel coating, endowing the enzyme-nanogels system with adaptive structure and functional properties.[39,40] With enhanced enzymatic stability and functionality, this method has broadened the applicability of enzymes to different biomedical applications, such as cancer therapy, central nervous system diseases, ischemia, and reperfusion injury. [9,40–43].

Herein, we aimed to construct a silver-enzyme nanogels assembly, which was formed by a metal ion–imidazole coordination method to promote diabetic wound healing by continuous

cascade multi-functional reactions **(Scheme 1)**. GOX, HRP and CAT were carefully chosen as the therapeutic agents. Through polymerization on the surfaces of three selected enzymes, we successfully obtained imidazole-modified enzyme nanogels. The enzyme nanogels were then assembled into clusters through the coordination between silver ions and the imidazole groups. High level of glucose was effectively consumed by GOX, while the product H_2O_2 was then partially degraded to oxygen by CAT and oxidized to toxic •OH by HRP. Altogether, our multi-enzymes cascade system can realize glucose consumption, •OH generation against bacterial infection as well as continuous oxygen production. The armored polymer nanogel conferred adaptability to the enzymes, enabling their intact structures and stable enzymatic activity against challenging bioenvironmental conditions and long-term storability. Meanwhile, silver ions as a potent anti-bacterial component were utilized as the coordination ligand to bridge three distinct enzyme nanogels.[44,45] This design ensured triple enzymes function in tandem and accelerate the cascade reactions with substrates moving within the assembly. The cluster structure, enzyme stability, *in vitro* and *in vivo* enzyme activity as well as the therapeutic effect of the materials in bacterial test and rat models were systematically studied and evaluated. This study has proved that our silver-enzyme nanogels assembly could synergistically achieve effective diabetic wound healing, with adaptability, hypoxia-alleviated, anti-hyperglycemic, antimicrobial, anti-inflammatory, and angiogenic properties. While few studies of enzyme-based nanodrugs were reported to accomplish such multifunctional features, our materials endowed with biocompatible and effective wound healing properties, provide a promising strategy to develop clinical infected diabetic skin wound enzyme-drug and can be further applied in wound dressing materials.

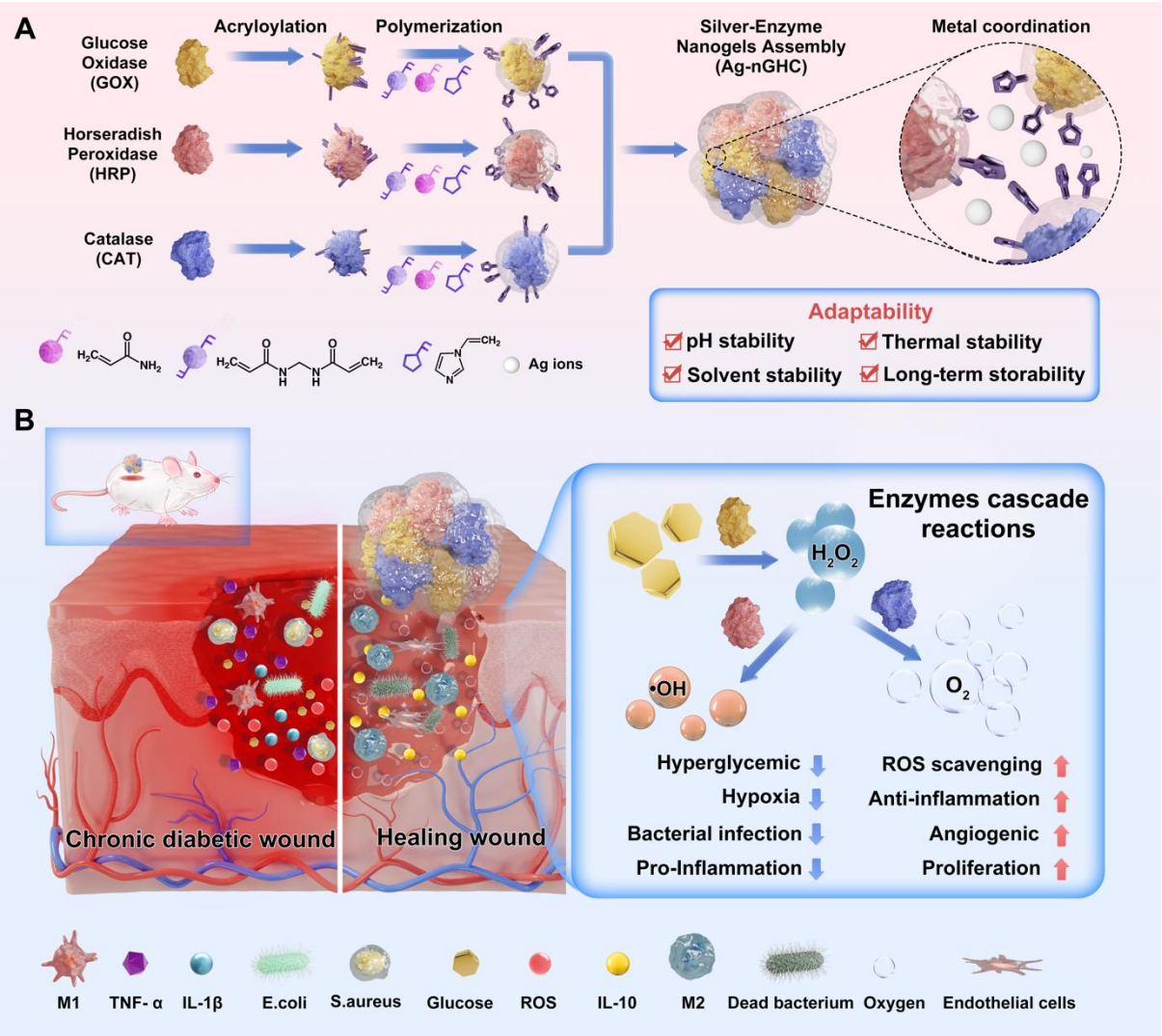

Scheme 1. Schematic illustration of A) silver-enzyme nanogels assembly (Ag-nGHC) synthesis and B) its functions in targeting complicated chronic diabetic wound healing.

2. Results and Discussion

2.1 Synthesis and structure characterization of silver-enzyme nanogels assembly

To confirm the formation of enzyme nanogels as well as their cluster upon coordination with silver ions, Fourier Transform Infrared (FTIR) spectroscopy was utilized to compare the spectra of native enzymes (GHC), three enzyme nanogels (nGHC), and silver-enzymes nanogels assembly (Ag-nGHC), as illustrated in **Figures 1A**. Typically, protein possesses two discernible peaks in the FTIR spectrum, the Amide I (around 1650 cm^{-1}) and Amide II (around 1540 cm^{-1}), with the latter one being associated with N-H bending of the peptide backbone.[46] For enzyme acryloylation, N-acryloxysuccinimide (NAS) was employed to react with the amino groups on the enzyme surface, realizing the introduction of vinyl groups. This modification resulted in a notable decrease in the peak absorption density at 1544 cm^{-1} in both nGHC and Ag-nGHC. The outer layer of enzyme nanogels comprised a polyacrylamide and imidazole network. The appearance of a new absorption peak at 1043 cm^{-1} for the synthesized materials corresponds to the aliphatic amide bond on the polyacrylamide side chains.[47] Additionally, spectral bands at 1188 cm^{-1} arose due to $–NH_2$ rocking vibrations bonded on the polymer chain.[48,49] The absorption bands at 1088 cm^{-1} and 1414 cm^{-1} were ascribed to bending / stretch modes and skeleton vibrations of the imidazole ring, respectively.[50] Similar absorbance changes could also be observed in separated nature enzymes and nanogel-encapsulated enzymes (**Figure S1**). Imidazole group is well-known for its capacity to coordinate with metal ions. To examine the coordination between the imidazole group and silver ions, the FTIR spectrum of nGHC and Ag-nGHC was meticulously compared. In addition to the similar absorption peaks, a distinct new peak at 1383 cm^{-1} was observed, attributable to the metal–ligand interactions and electron transfer. [51,52]

The variations of zeta potential and hydrodynamic particle sizes in the synthesis process for Ag-nGHC were depicted in **Figure 1B** and **Figure 1C,** respectively. The acryloylation of enzymes led to a more negative charge (-17.3 mV) compared to the native enzymes (-10.5 mV), while the surface potential changed to -1.58 mV after polymerization. Notably, silver chelation for cluster formation further increased the surface charge to 4.81 mV. Positively charged particles have been proven to facilitate attachment to both gram-positive and gram-negative bacterial membranes, which typically exhibit negative surface potentials. This electrostatic interaction generates an interfacial potential effect, thereby enhancing the antimicrobial efficacy. Moreover, dynamic light scattering (DLS) data indicated that nGHC possessed a

larger hydrodynamic diameter (ranging from 8.3~20.5 nm) due to the polymer network enveloping the enzymes, as compared to free enzymes GHC (4.5~15.1 nm), as depicted in **Figure 1C**. A similar increment in particle size was corroborated for three distinct enzymes and their respective nanogel counterparts, as evidenced in **Figure S2**. Upon coordinating with silver ions, a comparative escalation in particle size to around 768 nm was observed. Moreover, the particle size could be adjusted by changing the amount of silver ions. At low concentrations of silver ions added, the particle size increased to around 100 nm (25 μM). With the addition of silver ions, the enzyme nanogels gradually formed into larger assemblies. If the silver ion concentration increases to 150 μM, the particle size increases to 1155 ± 153.5 nm. **(Figure S3)** The conformation of enzyme structures upon nanogel encapsulation and silver coordination was further evaluated by circular dichroism (CD). CD spectrum (**Figure S4**) suggested no significant change in enzyme secondary structure, which indicated polymerization and coordination presented no adversary effects on protein structures.[36]

Scanning electron microscopy (SEM) image revealed the Ag-nGHC assembly, as shown in **Figure 1D**, exhibited a spherical structure, congruent with the morphological characteristics observed in transmission electron microscopy (TEM) image (**Figure 1E**). Furthermore, the TEM-EDS mapping (**Figure 1F**) confirmed the existence and uniform distribution of silver, oxygen, and nitrogen elements on the Ag-nGHC surface. Oxygen and nitrogen elements came from enzymes themselves. This observation further supported that silver ions acted as binding agents to bridge the enzyme nanogels.

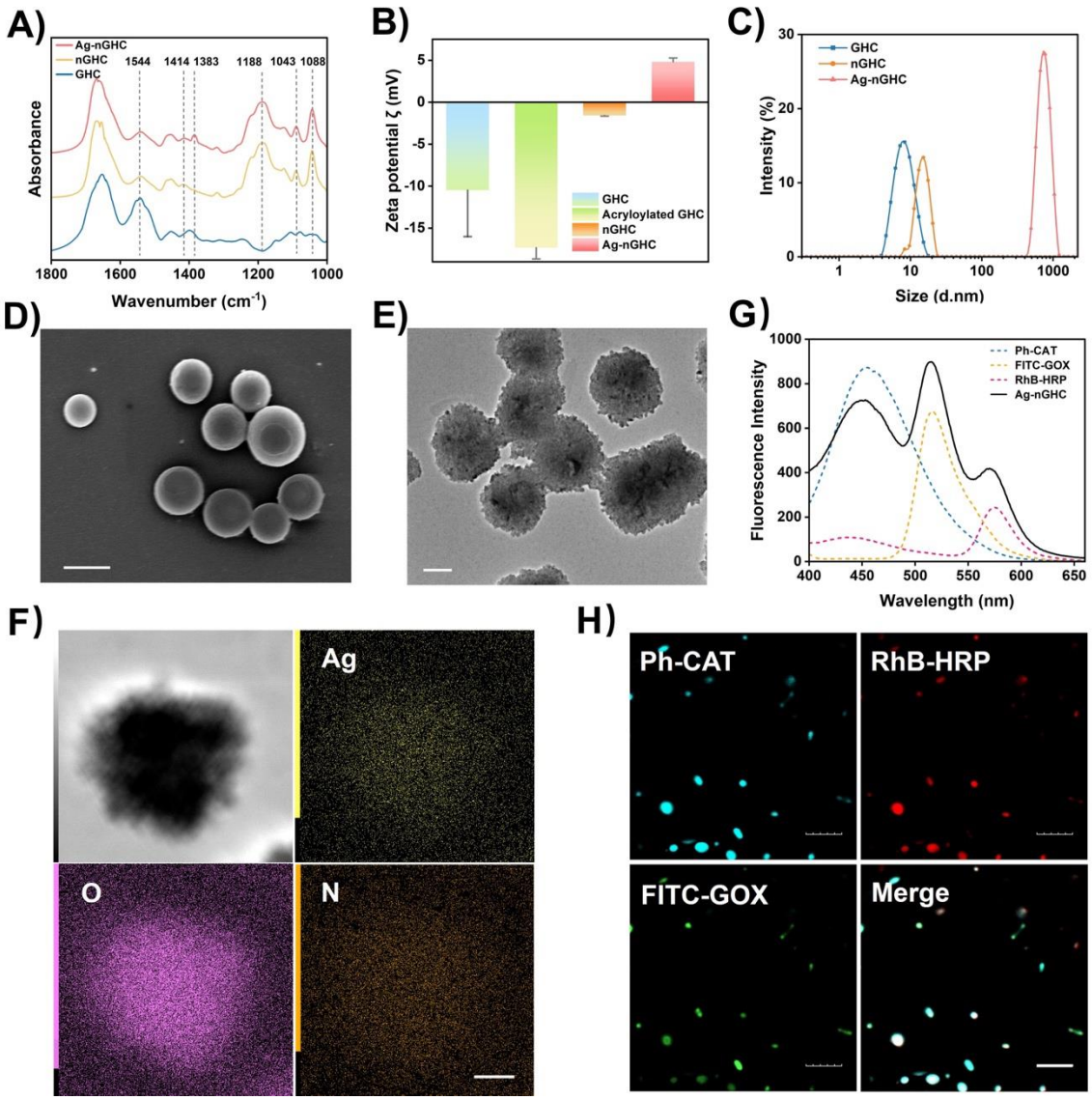

Figure 1. Structure and morphology of silver-enzyme nanogels assembly. A) FTIR absorbance spectra of natural GOX-HRP-CAT enzymes (denoted as GHC), three enzyme nanogels (denoted as nGHC), and silver-enzyme nanogels assembly (denoted as Ag-nGHC). B) Zeta potential of GHC, acryloylated GOX-HRP-CAT (denoted as acryloylated GHC), nGHC and Ag-nGHC which indicates the self-assembly of the clusters. C) DLS results of particle sizes of GHC, nGHC and Ag-nGHC. D) SEM image of Ag-nGHC. (Scale bar: 1 μm) E) TEM image of Ag-nGHC. (Scale bar: 200 nm) F) TEM EDS images of Ag, N and O elements, where Ag ions spread around the surface of the Ag-nGHC (Yellow: Ag, Pink: O, Orange: N). (Scale bar: 200 nm) G) Fluorescence spectra of FITC-GOX, RhB-HRP, Ph-CAT and Ag-nGHC at excitation wavelengths of 350 nm. H) Confocal microscopy images of Ph-CAT, FITC-GOX, RhB-HRP and merge. (Scale bar: 5 μm) The bar graphs represent mean ± SD.

Multienzyme immobilization serves as a potent strategy to fabricate cascade enzymatic pathways, offering a multitude of benefits. This approach facilitates cascade reactions within compact and small reactor systems, augments flow reaction rates and reduces the duration of reaction cycles.[53] Homogenous distributions of trienzymes within the silver coordinated nanogel clusters were studied through fluorometer and confocal laser scanning microscopy (CLSM). To distinguish three enzymes within Ag-nGHC, GOX, CAT, and HRP were labeled with fluorescein isothiocyanate (FITC), phthaldialdehyde (Ph) and rhodamine B isothiocyanate (RhB), respectively, to monitor their spatial relations under fluorescence spectrometer and confocal microscope. As shown in **Figure 1G**, emission peaks were detected at 450 nm, 515 nm and 575 nm for single Ph-CAT, FITC-GOX, and RhB-HRP, respectively, under the same excitation wavelength at 350 nm. Upon coordination with silver ions, the intensity at 450 nm decreased because part of the fluorescence resonance energy was absorbed by the FTIC and RhB molecules as their excitation energy. Accordingly, increased intensity at emission wavelengths of 515 nm and 575 nm on fluorescence spectrum were observed due to this fluorescence resonance energy transfer (FRET) effect of three adjacent enzymes. This supported our methods that successfully encapsulated three enzymes. Additionally, confocal microscopy images of Ag-nGHC **(Figure 1H)** clearly revealed Ph-CAT, RhB-HRP and FITC-GOX under different excitation wavelengths, emitting blue, red and green fluorescence. The merged fluorescent image further demonstrated the homogeneous loading of three florescence-labeled enzymes within the same clusters. Hence, the successful confinement of three enzymes can be confirmed, which will further enhance the catalytic reaction rate via substrate channeling and enzyme stability.

2.2 *In-vitro* enzymatic activity assessment

The silver-enzyme nanogels assembly enables the combination of several cascade chemical processes in the proximity of the self-assembled nanogels, which further boost catalytic reactions.[53,54] The expected cascade reactions are illustrated in **Figure 2A**, where the excess glucose around the diabetic wound site would be quickly consumed by GOX. Afterward, the produced H_2O_2 can be further catalyzed to generate •OH by HRP and O_2 by CAT, respectively. The consumption of glucose could modulate the wound environment by alleviating hyperglycemia conditions, and the formation of toxic •OH could kill microbial, controlling potential microbial contamination. Meanwhile, the generation of oxygen could improve the hypoxic environment in the wound site and facilitate wound healing.

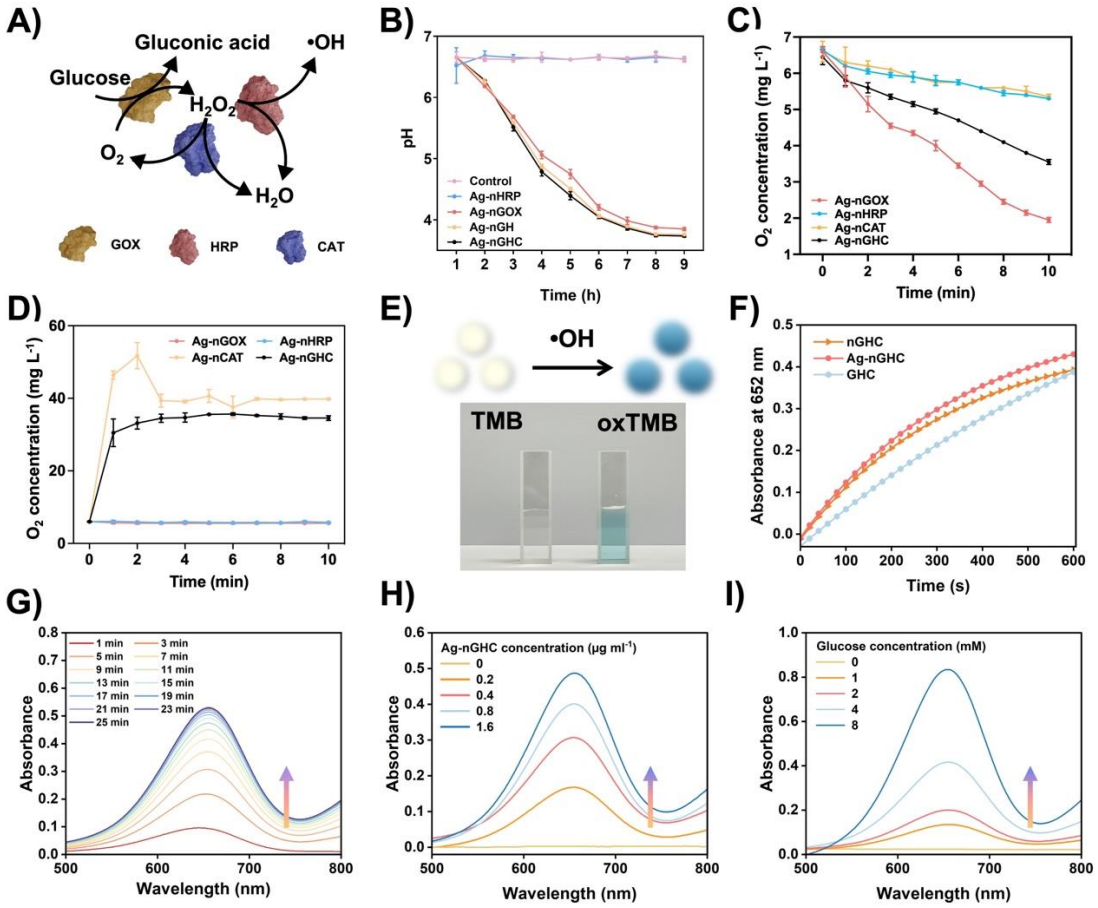

Figure 2. *In vitro* enzymatic test of Ag-nGHC assembly. A) Cascade reactions within Ag-nGHC assembly. B) pH variation under the treatment of different components: control, Ag-nGOX, Ag-nHRP, Ag-nGOX-HRP (denoted as Ag-nGH) and Ag-nGHC in the presence of 5 μg mL^{-1} glucose. C) O_2 variation under the treatment of different components: Ag-nGOX, Ag-nHRP, Ag-nCAT and Ag-nGHC in the presence of 5 μg mL^{-1} glucose. D) O_2 variation under the treatment of different components: Ag-nGOX, Ag-nHRP, Ag-nCAT and Ag-nGHC in the presence of 1% H_2O_2. E) Schematic illustration of •OH reaction with TMB and its colour variation. F) Monitored UV absorbance of TMB oxidation kinetics treated with GHC, nGHC, and Ag-nGHC at 652 nm under the same glucose concentration (4 mM). G) UV Spectra of TMB solution oxidized by Ag-nGHC (0.4 μg mL^{-1}) over a 23-minute reaction period with 4 mM glucose. H) Variation in UV spectra of TMB solution oxidized by Ag-nGHC at different concentrations of 0, 0.2, 0.4, 0.8, and 1.6 μg mL^{-1} with 4 mM glucose for 5 minutes. I) Variation in UV-Vis spectra of TMB solution oxidized by Ag-nGHC (0.4 μg mL^{-1}) with different glucose concentrations of 0, 1, 2, 4, and 8 mM for 5 minutes. The bar graphs represent mean ± SD.

The production of gluconic acid will lead to acidification of the solution. Accordingly, pH serves as a reliable indicative for gauging glucose utilization, as evidenced in **Figure 2B.** With the addition of GOX, pH values in glucose solution were observed to decrease significantly (dropped from 7 to around 3.5 within 10 hours) compared with the group without GOX (Ag-nHRP and glucose treatments) where the pH values remained stable. Additionally, Ag-nGHC and glucose concentrations were further explored to evaluate the pH variation, as shown in **Figure S5**. An increased concentration of Ag-nGHC in the solution corresponded with a more rapid decline in pH, descending below 4.5 within 240 minutes. To mimic the different glucose levels within healthy tissues and diabetic tissues, two concentrations of glucose,100 mg dL^{-1} and 400 mg dL^{-1}, were employed. At the diabetic tissue-simulating concentration of 400 mg dL^{-1}, a precipitous pH reduction was observed within the first two hours, followed by a relatively stable pH value at around 3.4. Conversely, at a glucose level representative of healthy tissue, the pH slowly decreased, achieving a value of 4.1 throughout a four-hour reaction period. These results indicated that GOX functioned efficiently to oxidize glucose.

In diabetic patients, impaired blood flow often leads to hypoxia in the wound area, which can significantly hamper the healing process. Adequate oxygenation is essential for various stages of the wound healing process, including inflammation, new tissue formation, and remodeling.[55] The CAT can lead to H_2O_2 decomposition and replenish the O_2 supply for glucose oxidation. As compared to the GOX-treated group in **Figure 2C**, the oxygen concentration remained at a relatively higher level by using Ag-nGHC in the glucose solution. Meanwhile, in the presence of a 1% H_2O_2 solution, both Ag-nCAT and Ag-nGHC greatly increased the dissolved oxygen concentration above 35 mg L^{-1} within a short time, as depicted in **Figure 2D**. These results together suggested using CAT can facilitate to alleviate hypoxia at the wound site, therefore, promoting the healing process.

To evaluate the generation of •OH catalyzed by HRP, 3,3′,5,5′-tetramethylbenzidine (TMB) was utilized as an indicator of •OH, as illustrated in **Figure 2E**, where oxidized TMB (oxTMB) with blue color yield a distinct absorption peak at 652 nm. In **Figure 2F**, Ag-nGHC showed the highest catalytic rates in comparison with nGHC and free enzymes, which may be attributed to the substrate channeling formation upon trienzyme co-immobilization by silver ions.[53] The close distance among enzymes facilitates the substrate transfer and protects the unstable intermediates. The optical absorption band at 652 nm of oxTMB was gradually intensified with reaction time reaching up to 23 min after applying Ag-nGHC and glucose in the TMB solution

(**Figure 2G**). Then, the corresponding absorbance values at 652 nm of silver-enzymes catalytic system towards various concentrations of Ag-nGHC and glucose were investigated under different experimental conditions. As shown in **Figure 2H** and **Figure 2I**, with the increase of sample concentration ranging from 0 to 1.6 μg mL^{-1}, the UV-vis absorbance intensity gradually increased at 652 nm in the same reaction time intervals. Similarly, an increased trend was detected with elevated concentration of glucose from 0 to 8 mM. The above experiments indicate that the synthesized Ag-nGHC composite did not affect the activity of related enzymes.

2.3 Kinetics and stability performance of silver-enzymes nanogels assembly

To better understand the enzyme catalytic behaviour, the kinetics of three enzyme nanogels and their native enzymes were studied (**Figure S6**), with detailed kinetic parameters listed in **Table S2.** Following the modification with polyacrylamide and coordination with silver ions, the Michaelis Constant (K_m) of the three enzyme nanogels increased compared to their native counterparts. This suggests that the polymerized enzyme nanogels require a higher substrate concentration to achieve their maximum reaction rate, likely due to the thin polymer network and cluster formation affecting substrate transit into the interior enzymes. The catalytic efficiency (k_{cat}/K_m) values for all enzyme nanogels and native enzymes were also calculated. All GOX, HRP and CAT retained above 80 % of their original activity after encapsulation with the polymer. These kinetic parameters demonstrate that the thin polymer layer and coordination with silver ions did not significantly impact enzyme activity or substrate transit to the active sites of the enzymes, facilitating the subsequent diabetic wound healing applications.

We then investigated the stability of the enzyme nanogels against different external stimuli. Previous research showed that high temperatures (above 50 °C) can alter the structure of enzymes, reducing their catalytic ability, which may limit the transportation and storage of enzyme-based materials in clinical use.[36,56] To illustrate the thermal stability of the enzyme nanogels, we compared their catalytic performance at elevated temperatures with that of free enzymes. As shown in **S7A**, Ag-nGHC retained their enzymatic activity at above 80% even as temperatures rose up to 65 °C, in stark contrast to the free enzyme cascade system which lost about nearly 90% of its activity under the same conditions. Besides thermal stability, the nanogels were also proven to improve enzyme stability under different pH environments. Ag-nGHC exhibited higher catalytic activity at 62.8% under alkaline environments (pH=8), while the catalytic activity of free enzymes only remained at 23.2%. **(Figure S7B)** The enzymatic stability was further confirmed by sustained activity over seven days of storage at ambient

temperature. The relative activities of Ag-nGHC decreased slowly to 67.7% with time while the free enzymes experienced a precipitous decline in activity, retaining merely 37.7% after seven days, as depicted in **Figure S7C**. The experiments above demonstrated the enzyme nanogels cluster exhibited excellent pH tolerance, thermostability and long-term storability.

To further evaluate the enzymatic stability during the drug delivery process and transportation, corresponding compounds were applied to stimulate the *in vivo* bioenvironment. Proteolytic degradation and chelation-induced inactivation, as two predominant factors, affected enzyme stability *in vivo*.[57] Thus, the stability of Ag-nGHC and free enzymes GHC was investigated in the presence of these representative chemical compounds: trypsin and ethylenediaminetetraacetic acid (EDTA) (**Figure S7D**). The free enzymes incubated in trypsin solution (proteolytic enzymes) lost around 51.0% of their overall enzymatic activity whereas the Ag-nGHC remained up to 87.4% relative activity under the same treatment. Similarly, higher activity remained of Ag-nGHC (86.9%) in the presence of EDTA, compared to that of free enzymes (52.9%). The enhanced stability of Ag-nGHC was ascribed to the polymer networks coated on the surface of enzymes, which could shield the enzymes and mitigate enzyme denaturation.[54,58] Another rationale is that the silver-induced aggregations protect the inner enzymes from directly reacting with harsh environments. Consequently, nanogel encapsulation and self-assembly processes appear to be advantageous strategies for protecting enzymes, enhancing their clinical applicability.

2.4 The anti-bacterial effect of Ag-nGHC assembly

Bacterial infection is considered to be one of the main obstacles to the early diabetes mellitus healing stage.[19] High levels of glucose are conducive to bacterial growth, therefore, targeting glucose consumption could be a promising strategy to combat bacterial infection. GOX can act as a powerful anti-bacterial agent to consume glucose and produce high levels of hydrogen peroxide. HRP, another catalytic enzyme that transfers hydrogen peroxide into toxic compound •OH, exhibited enhanced anti-bacterial properties with GOX. Moreover, the contained silver ions have also been proved to greatly reduce the proliferation activity of bacteria by disrupting the bacterial cell membrane's permeability, inactivating proteins through binding with sulfhydryl groups, leading to oxidative stress, and interfering with DNA replication.[44]

The anti-bacterial behavior of Ag-nGHC was comprehensively evaluated *in vitro* studies. Antibacterial experiments were conducted using gram-positive Staphylococcus aureus

(S.aureus) and gram-negative Escherichia coli (E.coli) as model bacteria. As shown in **Figure 3A**, the bacterium grew dramatically without drug treatment. In comparison, the ones treated with Ag-nGH, which contained both GOX and HRP, showed the most significant anti-bacterial effect in both E.coli and S.aureus groups. The Ag-nGOX and Ag-nGHC groups also exhibited strong bacterium-killing ability. The optical density at 600 nm (OD600) results **(Figure 3B and 3C)** also indicated that the GOX-contained group had a significant inhibitory effect on these bacteria. We also conducted the live-dead staining analysis of bacteria. As shown in **Figure S8**, the silver-enzyme nanogel group exhibited strong antibacterial effects, evidenced by a significant decrease in green fluorescence intensity and an increase in red fluorescence intensity. Compared to the blank control group, the green fluorescence in the Ag-nCAT and Ag-nHRP groups decreased, indicating that silver ions have an inhibitory effect on bacteria. This is also aligned with the results in **Figure 3A,** where the group treated with Ag-nCAT exhibited the bacteria-killing effect. However, the Ag-nGH and Ag-nGHC groups demonstrated the most potent antibacterial effect. It shows that its antibacterial effect mainly comes from highly toxic free radicals generated by enzyme cascade reactions.

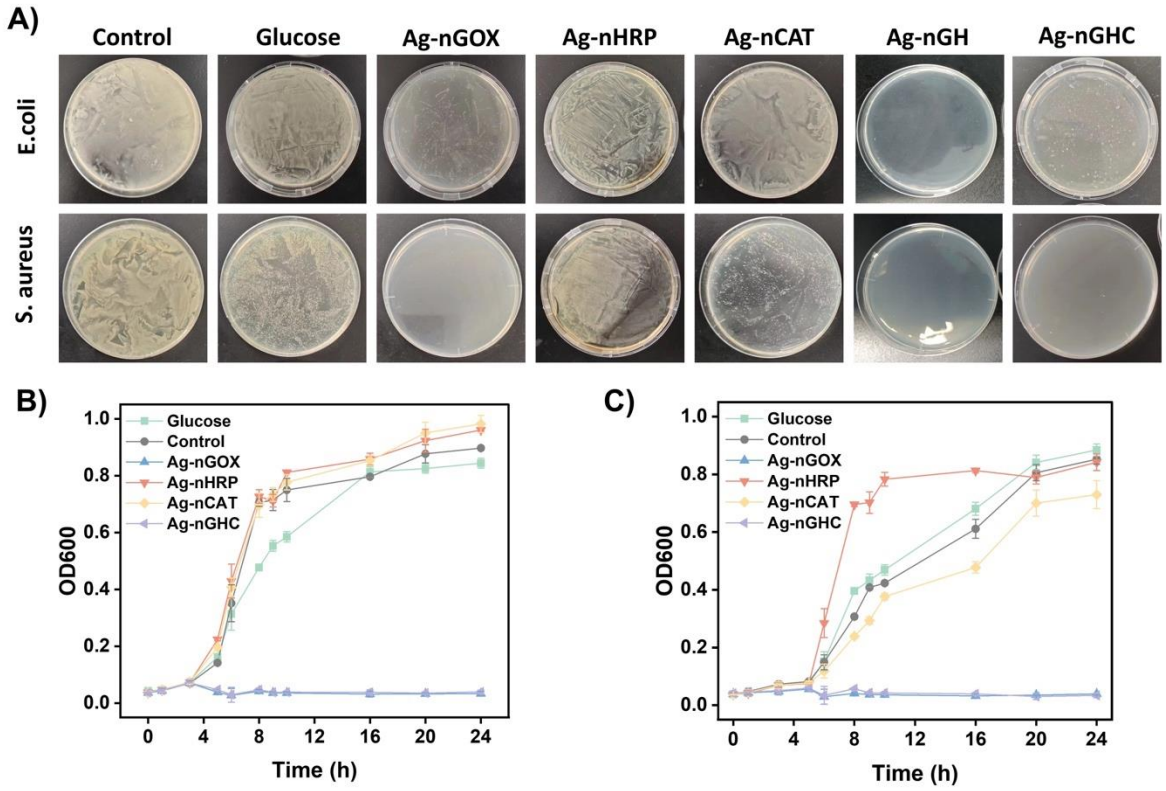

Figure 3. Evaluate the anti-bacterial property of the Ag-nGHC assembly. A) Representative images of E. coli and S. aureus bacterial clones on LB-agar surfaces under different treatments. B) Changes in E. coli OD600 concentration in different treatment groups. C) Changes in

S.aureus OD600 concentration in different treatment groups. The bar graphs represent mean ± SD.

2.5 Cytotoxicity evaluation and antioxidant/oxygen supply effects of Ag-nGHC assembly

As shown in **Figure 4C**, the cytotoxicity of different groups of drugs on cell lines was tested using an MTT assay. The cell viability of Ag-nGOX assembly gradually decreased to only 29.8% as the applied concentration increased to 12.5 μg mL^{-1}, which may be caused by the gluconic acid produced by GOX and the high concentration of hydrogen peroxide by-products. At a high concentration of 12.5 μg mL^{-1}, cells treated with Ag-nHRP possessed a survival rate of over 95% with almost no cytotoxicity, while Ag-nCAT exhibited an even stronger promoting effect on cell growth. Ag-nGHC materials also showed the effect of promoting cell growth under different concentrations, possibly because CAT can quickly decompose H_2O_2 to prevent its toxic side effects on cells and produce oxygen to enhance the microenvironment to promote cell growth.

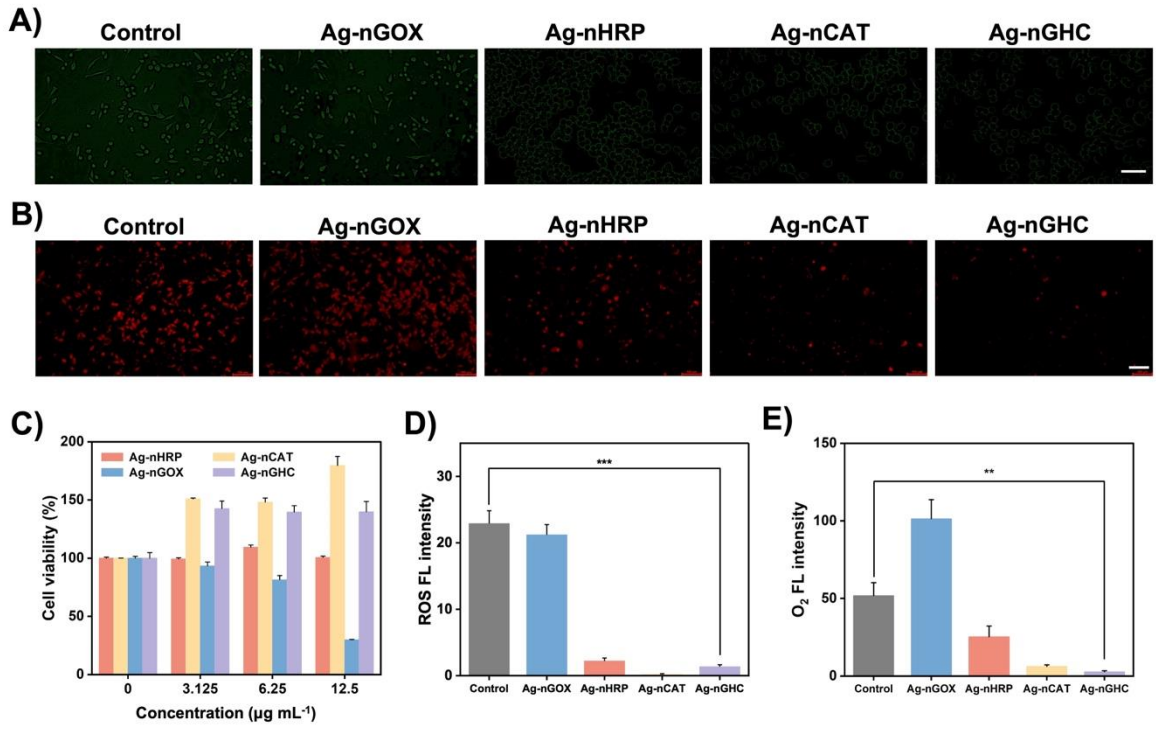

Figure 4. Oxidative states verification of silver-enzyme nanogels assembly. A) Representative images of alleviation of oxidative stress in L929 cells treated with different silver-enzyme nanogels via a ROS probe (DCFH-DA). (Scale bars: 100 μm). B) Representative images of intracellular O_2 generation after FBS-free DMEM and different silver-enzyme nanogels treatment of L929 cells, validated by the O_2 probe $[Ru(dpp)_3]Cl_2$. (Scale bars: 100 μm). C) Cell

viability under different treatments of Ag-nHRP, Ag-nCAT, Ag-nGOX, and Ag-nGHC. D) The relative fluorescence intensity of intracellular ROS. E) The relative fluorescence intensity of intracellular O_2. The bar graphs represent mean ± SD. ***p<0.001 **p<0.01.

Additionally, sustained oxidative stress causes the senescence of key healing cells, including fibroblasts, endothelial cells, keratinocytes, and mesenchymal stem cells, significantly impairing the healing process, such as granulation tissue formation, blood vessel creation, and epithelium regeneration.[12] We assumed that our materials could alleviate this oxidative environment, as both HRP and CAT can decompose H_2O_2. As shown in **Figure 4A and Figure 4D**, the intracellular ROS level of L929 cells which reflected the intracellular oxidative stress state was detected using ROS probe DCFH-DA. The results indicated that the Ag-nGHC material possessed good ROS consumption ability. In addition, as shown in **Figure 4B and Figure 4E**, we also investigated the intracellular oxygen level to verify the ability of our material to produce oxygen. After incubation with $[Ru(dpp)_3]Cl_2$, the red fluorescence intensity in L929 cells was significantly high with a value of 51.85. However, after treatment with the Ag-nGHC, due to sufficient oxygen produced by Ag-nGHC can act to quench the red fluorescence, the relative fluorescence signal value decreased to 2.75. This result was aligned with the previous *in vitro* study, indicating that Ag-nGHC can effectively promote oxygen supply inside the cells.

2.6 Macrophage polarization and anti-inflammatory effects by Ag-nGHC

Research extensively reviews the timing and role of macrophages in wound healing, highlighting differences between normal and diabetic conditions. In typical wound healing, M1 macrophages dominate early on (day 1 to day 3), initiating the inflammatory phase, with a subsequent shift towards M2 macrophages, which promote healing and peak around day 7.[59] However, in diabetic wounds, this transition is impaired: M1 macrophages persist regardless of the healing stage, contributing to chronic wound conditions.[60] The presence of M2 macrophages, generally considered pro-healing, suggests that promoting their predominance could enhance wound healing. Hyperglycemia promotes M1 polarization by increasing pro-inflammatory cytokines, such as TNF- α, IL-1, and IL-6. These cytokines, more prevalent in high-glucose conditions, enhance the metabolic activity of M1 macrophages, creating a feedback loop that exacerbates macrophage activation and inflammation.[61] Moreover, excessive ROS can promote continuous pro-inflammatory cytokine secretion and impair the function of dermal fibroblasts and keratinocytes, further hindering wound healing. Hence, this

impaired switch from M1 to M2 macrophages in diabetic wounds leads to delayed wound closure, poor angiogenesis, and reduced collagen deposition. Therefore, we speculated that ameliorating the hyperglycemic and high oxidative stress wound environment can change the imbalance existence of macrophage phenotype and the secretion of inflammatory factors.

Herein, lipopolysaccharide (LPS) induced inflammation cells were used as a comparison. As shown in **Figure 5A** and **Figure 5B**, the flow cytometry results indicated that the Ag-nGHC system could indeed reduce LPS polarized M1 macrophages to 33.2% and significantly increase the proportion of M2 macrophages from 5.9% to 36.3%. We also performed immunofluorescence staining to analyze the phenotype of nanogel-treated macrophages. The results (**Figure S9**) further demonstrated that the silver-enzyme nanogel-treated groups containing CAT effectively resisted LPS-induced macrophage polarization towards an anti-inflammatory phenotype. Additionally, the results (**Figure 5C-5E**) revealed notable alterations in cytokine expression levels with the introduction of the Ag-nGHC system. Specifically, there were substantial reductions in the levels of both pro-inflammatory cytokines TNF-α and IL-1β. This decrease suggested a mitigated inflammatory response. Concurrently, the expression of the anti-inflammatory cytokine IL-10 was significantly elevated, which was indicative of an enhanced anti-inflammatory response.

Our findings indicated that Ag-nGOX promotes the polarization of macrophages towards the M1 phenotype. This is beneficial in the early stages of wound healing where a robust inflammatory response is necessary to combat bacterial infection. Ag-nCAT and Ag-nGHC promote the polarization of macrophages towards the M2 phenotype, which is essential for resolving inflammation and facilitating tissue repair and regeneration in the later stages of diabetic wound healing. Meanwhile, changes in cytokine expression patterns implied that the Ag-nGHC system may effectively modulate macrophage activation states, shifting them towards the M2 phenotype that favored anti-inflammatory and tissue-repairing processes. In summary, the data supported the assumption that the Ag-nGHC clusters had the potential to orchestrate a beneficial shift in the chronic inflammatory wound microenvironment by modulating macrophage phenotypes and cytokine expression, thereby promoting a promote tissue repair and regeneration.

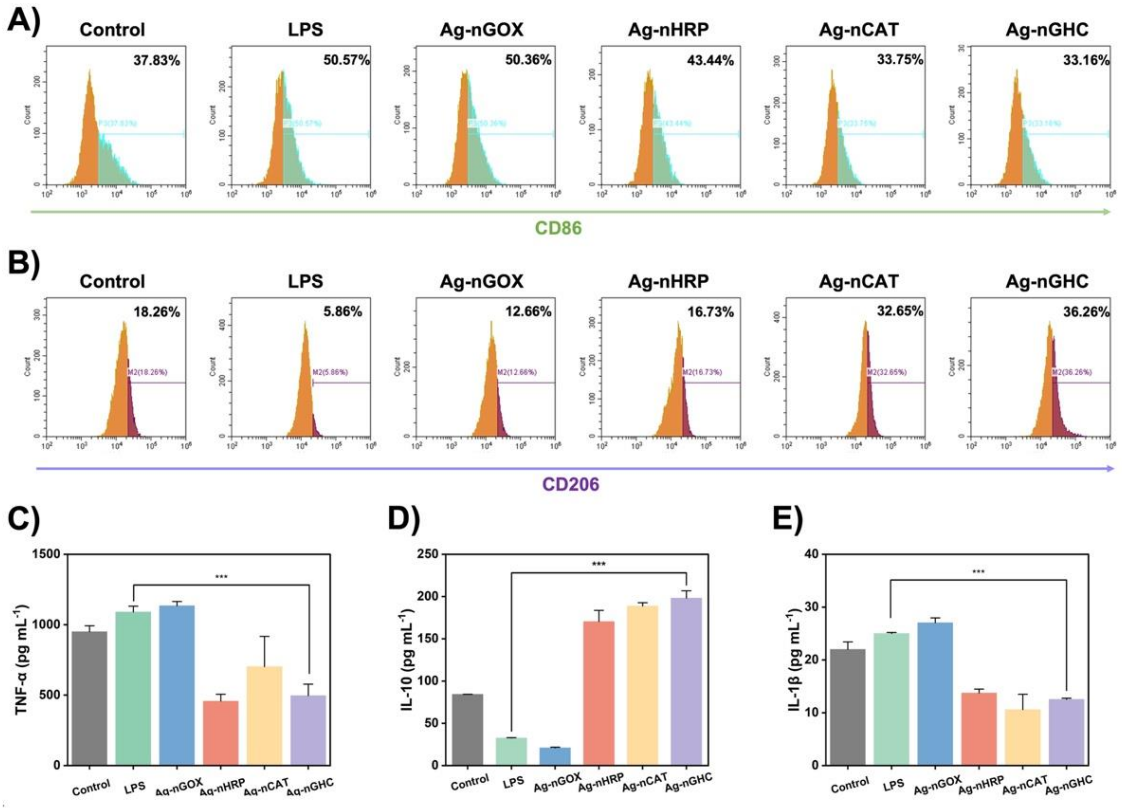

Figure 5. Immunomodulatory effect of Ag-nGHC assembly. A-B) Flow cytometry analysis of Ag-nGHC assembly reversing LPS-induced polarization of M1 macrophages and promoting M2 macrophages. (CD86: a marker associated with M1 macrophage activation; CD206: a marker associated with M2 macrophage activation) C-E) Statistical analysis of TNF-α, IL-10, and IL-1β levels during the diabetic wound inflammatory phase (n=3). The bar graphs represent mean ± SD. ***p<0.001.

2.7 Ag-nGHC assembly accelerated the healing of chronic wounds in diabetes *in vivo*

In order to further confirm the therapeutic role of Ag-nGHC assembly in accelerating wound healing of diabetes *in vivo*, we established a chronic wound model of diabetes SD rats infected with S.aureus for verification **(Figure 6A).** Tail vein blood glucose level was monitored to ensure that rats were in a hyperglycaemic state. Quantified contraction rates of the wound-healing area were further explored during the 14-day treatment period. Detailed histological studies using hematoxylin and eosin (H&E) staining were also conducted after the *in vivo* wound healing test to observe and understand the tissue characteristics.

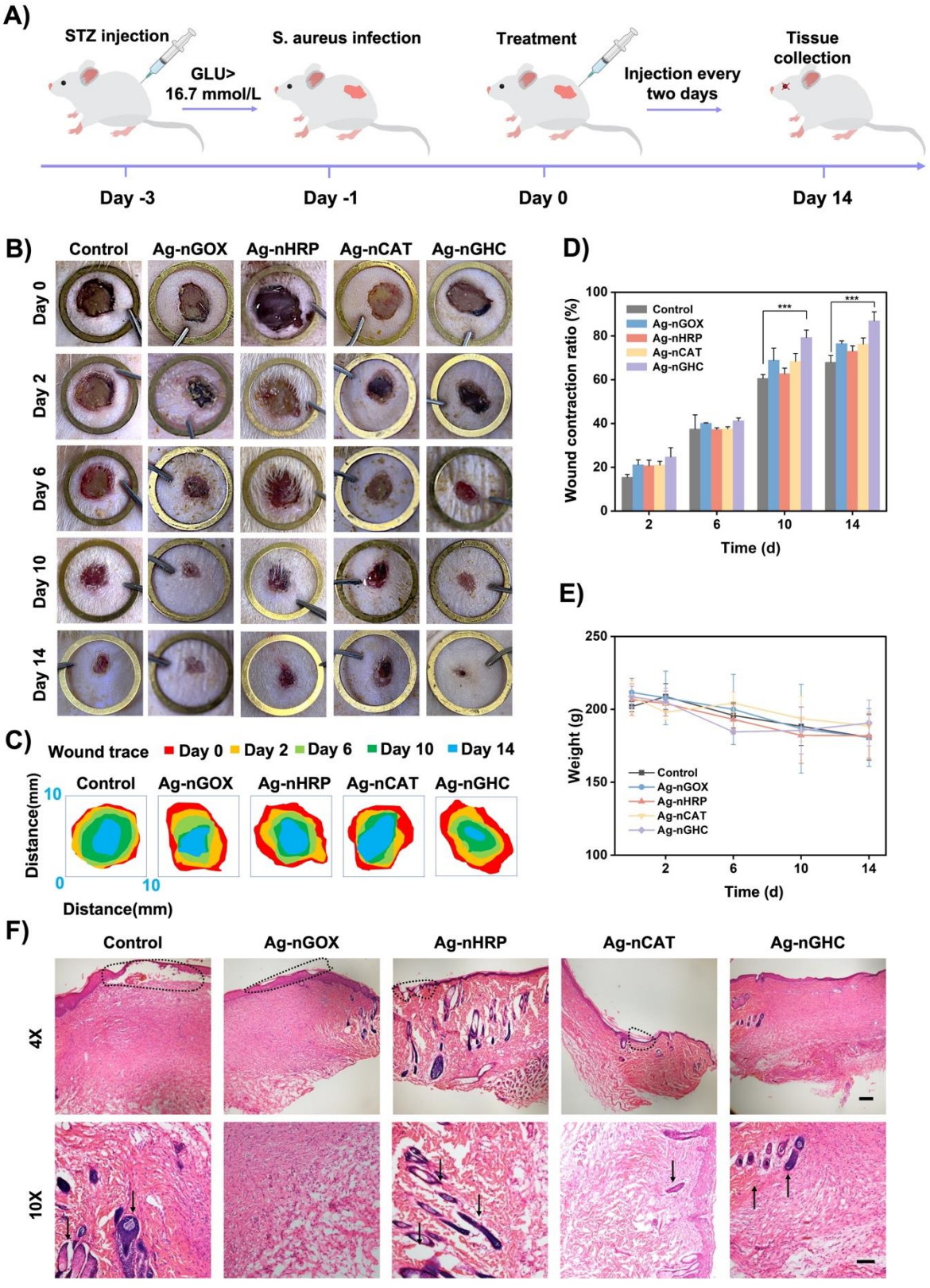

Figure 6. Ag-nGHC assembly promoted wound healing of diabetes *in vivo*. A) Schematic illustration of the timeline of diabetic rat experiments to verify the healing effect of Ag-nGHC. B) Images of the wound healing process of diabetes rats at different time points under different

treatments. (The diameter of the circular ring is 1.5 cm.) C) The traces of wound closure at different time points. (analyzed by PowerPoint software) D) Quantitative analysis of the wound contraction ratio. E) Monitored body weights of all diabetes rats under different treatments throughout the experiment. F) Histomorphological evaluation of wound regeneration was performed using H&E staining at two magnifications (dashed line: unhealed wound; black arrow, hair follicle). (4× image scale bar: 200 μm; 10× image scale bar: 100 μm). The bar graphs represent mean ± SD. ***$p<0.001$.

Figure 6B–D showed the progressive healing of wounds under different treatments over several time points, alongside a quantitative analysis of wound closure rates determined through wound size measurements. On day 10, wounds treated with Ag-nGHC demonstrated a significant healing advancement with a contraction rate of 79.27%, surpassing the control group's healing rate of 60.6%. The wound contraction trend continued until day 14, where the Ag-nGHC-treated group exhibited a mere average of 13.12% of the area remaining unhealed. In stark contrast, the diabetic control group continued to observe a considerably larger area of unhealed wounds. The body weights of rats were monitored during the whole treatment as shown in **Figure 6E**, no significant body loss was observed under different treatments. In addition, the H&E results (**Figure 6F**) indicated wound tissues treated with the Ag-nGHC had more hair regrowth and blood vessel formation, with no obvious unclosed wound area observed, indicating that its wound healing performance was better than that of the other groups. **Figure S10** showed no significant change in organ morphology under Ag-nGHC treatment, suggesting it was a safe therapeutic agent.

Finally, to further understand the wound microenvironment and repair mechanism under treatments, we detected ROS elimination in tissue slices to verify the *in vivo* wound oxidative stress state. **Figures 7A and 7B** depicted the fluorescence intensity associated with ROS in various groups. Notably, the fluorescence observed in the Ag-nGHC-treated tissues was markedly diminished in comparison to the control group. This suggested that the Ag-nGHC assembly had a pronounced capacity for scavenging ROS at the site of the wound, thereby mitigating the harmful effects of oxidative. Next, we evaluated neovascularization via CD31 immunostaining, as visualized in **Figures 7C and 7D**. The Ag-nGHC group displayed an impressive enhancement in red fluorescence, starkly outweighing that observed in the comparative groups. This significant increase in vascular formation spoke to the dynamic role

of Ag-nGHC in fostering an environment ripe for angiogenesis, a vital component for supplying essential nutrients and oxygen to the healing tissue.

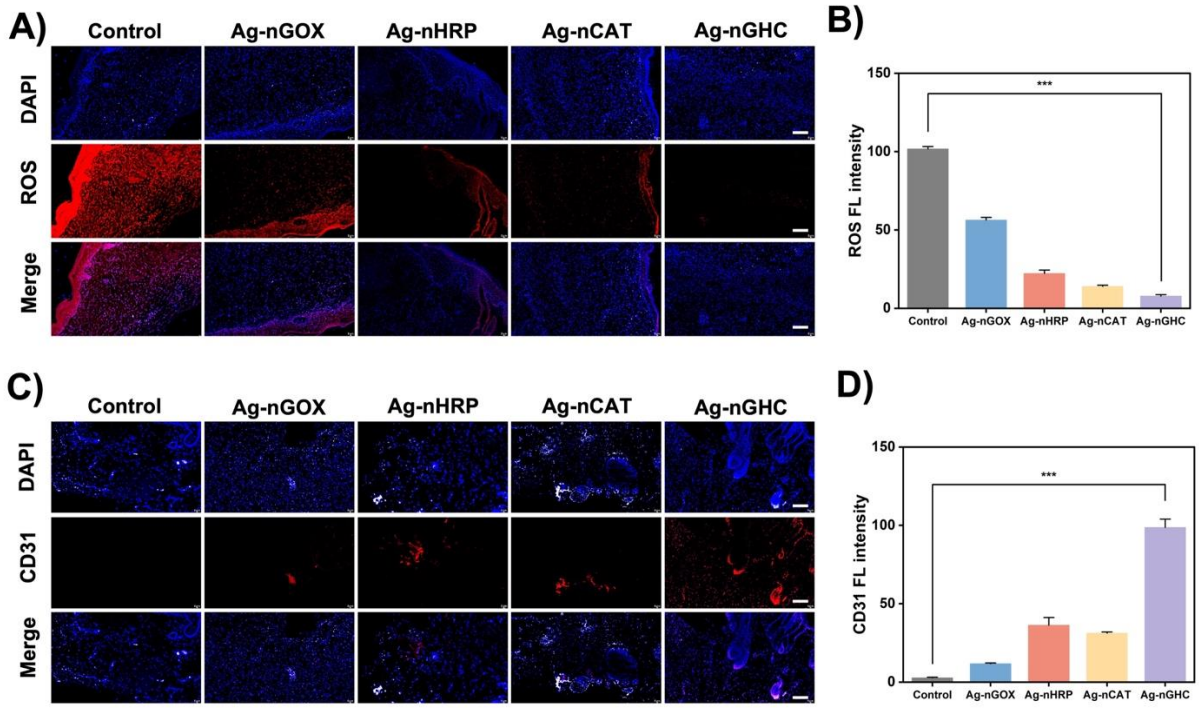

Figure 7. Oxidative stress alleviation and angiogenesis of Ag-nGHC assembly. A) Representative fluorescence images of ROS levels with DHE staining. (Scale bar: 50 μm) B) The relative fluorescence intensity of ROS. (Quantified using ImageJ software) (n = 3). C) Representative immunofluorescence images of blood vessel CD31-positive endothelial cells. (Scale bar: 50 μm) D) The relative fluorescence intensity of CD31. (Quantified using ImageJ software) (n = 3). The bar graphs represent mean ± SD. ***p<0.001.

To distill our findings, the Ag-nGHC assembly emerged as a multifaceted agent for diabetic wound remediation. It deftly tackled oxidative stress by robust ROS reduction, enriched the wound bed with necessary oxygen, and catalyzed the formation of new blood vessels. Together, these actions create a synergistic effect that significantly propels the pace of wound closure.

3. Conclusion

In summary, our research provides substantial evidence supporting the therapeutic efficacy of the silver-enzyme nanogels assembly (Ag-nGHC) in diabetic wound healing. The meticulous synthesis of three enzymes with outer polymer nanogel layers plays a crucial role in safeguarding the enzymes, substantially enhancing their adaptability and stability under a range

of challenging conditions. Our comprehensive *in vivo* and *in vitro* studies reveal that our material consistently improves and modifies the wound microenvironment. This is evidenced by alleviating hypoxia and hyperglycemia, generating hydroxyl radicals as well as additive anti-bacterial agent silver ions to combat bacterial infections by cascade reactions of three conjugated enzymes. These reactions favor the later processes such as re-epithelialization and angiogenesis throughout the healing trajectory. These findings affirm that Ag-nGHC provides a favorable niche microenvironment for diabetic tissue regeneration.

The application of this multi-enzyme nanodrug as a single therapeutic agent demonstrates notable benefits across various stages of the dynamic healing process. The properties of adaptability, anti-hyperglycaemic, hypoxia-alleviated, antimicrobial, anti-inflammatory, and angiogenic of Ag-nGHC enable it to overcome the limitations in targeting merely specific steps in wound healing under traditional treatment. Given its inherent characteristics, including anti-inflammatory and angiogenic properties, this enzyme nanodrug may also prove beneficial in treating other types of acute or chronic wounds, such as burn injuries, surgical incisions, and venous ulcers. Furthermore, it is imperative to undertake comprehensive investigations, exploring a broader range of materials suitable for specific disease contexts. These future studies should delve into detailed analyses of cell population migrations and signaling pathways, to fully harness the potential of this therapeutic approach.

4. Experimental Section

Materials: Glucose oxidase (GOX) from Aspergillus niger, catalase (CAT) from bovine liver, trypsin, acrylamide, N,N′-Methylenebis(acrylamide) (BIS), ammonium persulfate (APS), 3,3',5,5'-Tetramethylbenzidine (TMB), phthaldialdehyde (Ph), fluorescein isothiocyanate isomer I (FITC), Rhodamine B isothiocyanate (RhB), and mercaptoethanol were purchased from Sigma-Aldrich. Horseradish peroxidase (HRP), acrylic acid N-hydroxysuccinimide ester (NAS), 1-vinylimidazole, were obtained from TCI. N,N,N′,N′-Tetramethylethylenediamine (TEMED) was purchased from Bio-Rad Laboratories. Silver nitrate was purchased from Strem Chemicals (Singapore). All chemicals and solvents are analytical reagents and were utilized without further purification.

Preparation of acryloylated enzymes and fluorescence-labelled enzymes: The acryloylated enzymes were synthesized according to the previous method.[36,62] Specifically, GOX (50 mg) was dissolved in sodium carbonate buffer (13.5 mL, 20 mM, pH = 9.2). Then, NAS (1.5 mL, 80 mM) in DMSO solution was dropped into the above solution and stirred for 2.5 hours. The acquired solution was then dialyzed in DI water for 6 hours and adjusted pH to 7. Acryloylated HRP and acryloylated CAT were obtained using the same synthesis method.

To obtain acryloylated fluorescence-labeled enzymes, an additional FITC (2 mg) and RhB (2 mg) were mixed with GOX and HRP solution, respectively. For CAT labeling, Ph (2 mg) dissolved in DMSO and mercaptoethanol (200 μL) were added into the CAT solution for the synergic reaction. [63]

The number of acryloyl groups modified onto GOX, HRP and CAT surface was estimated by assessing the number of unreacted amino groups using a fluorescamine assay. Fluoresamine (3 mg mL-1) was dissolved in anhydrous DMSO. Both native and acryloylated GOX, HRP and CAT (1 mg mL-1) were prepared in HEPES buffer (0.05 M, pH 7.0). Subsequently, the fluoresamine solution (300 μL) was added to in enzyme solution (1 mL). The solution was incubated for 1 hour at room temperature (25°C). The average number of acryloyl groups attached to the enzymes was quantified by measuring the remaining unreacted lysine on the enzyme molecule using a fluoresamine assay."After incubation, the fluorescence intensity (Ex = 380 nm, Em = 480 nm) was measured using a fluorescence meter. On average, 9, 3, 12 of acryloyl groups were conjugated to the GOX, HRP and CAT. The research details were described in **Table S1**.

Synthesis of enzyme nanogels and silver-enzyme nanogels assembly: acryloylated enzymes or acryloylated fluorescence-labeled enzymes (10 mg) were further diluted to 1 mg mL^{-1} in

HEPES buffer (50 mM, pH=7), with acrylamide (20 mg) and 1-vinylimidazole (20 μL) added. BIS (7.2 mg) dissolved in DMSO (1 mL) was slowly dropped into the enzyme solution. Enzyme nanogels synthesis was initiated by mixing APS (2.2 mM) and TEMED (20 μL) at room temperature under a nitrogen atmosphere for a 2-hour reaction, followed by an 8-hour dialysis in DI water to remove all the unreacted compounds. The obtained enzyme nanogels were further diluted to 0.5 mg mL^{-1}, followed by an addition of silver nitrate (125 μM) at room temperature and reacted for 30 minutes to realize enzyme nanogel cluster formation. The solution was then diluted for another 8 hours to gain pure enzyme nanogels clusters.

Chemical structure and morphology characterization: Chemical functional groups of synthesized acryloylated enzymes, enzyme nanogels and silver-enzyme nanogels clusters were detected by Fourier-transform infrared spectroscopy (FTIR spectrometer: Agilent Cary 660). Dynamic light scattering (DLS: Malvern Zetasizer 26-21146) was carried out to measure both the hydrodynamic diameter and zeta potentials of the products in the suspensions. Scanning electron microscopy (SEM: Zeiss Supra 40) and transmission electron microscopy (TEM: JEOL 3010F) were utilized to obtain the morphology of silver-enzyme nanogels clusters. Energy dispersive X-ray spectroscopy (EDS) mapping was used to determine the elements on the silver-enzyme nanogels clusters. Circular dichroism (CD: Chirascan CD Spectrometer) was used to identify protein secondary structure change. To examine the multienzymes colocation, we used a spectrofluorophotometer (SHIMADZU RF-5301PC) to detect single fluorescence-labeled enzymes and fluorescence-labeled enzymes cluster at the excitation wavelength of 340 nm. Confocal microscopy (Olympus FV3000 Confocal Microscope) was conducted to visualize the colocation of silver coordinated- fluorescence labeled enzyme nanogels cluster (0.5 mg mL^{-1})

Evaluation of •OH generation in vitro: As HRP was capable of catalyzing H_2O_2 into •OH, which can cause TMB dye oxidation and induce UV signal variation, a solution of sample (0.4 μg mL^{-1}), glucose (4 mM), and TMB (10 μg mL^{-1}), was prepared in DI water, with a total volume of 1.5 mL. The reaction mixture was then incubated at room temperature. At various time points, oxidised TMB in the mixture was measured by a UV/vis spectrophotometer at a wavelength of 652 nm. The reaction rate was calculated by the absorbance variation:

$$Reaction\ rate\ (V) = \frac{A_t - A_0}{t}$$

(Where A_t represented the absorbance at 652 nm after a 5-min reaction, and A_0 represented the absorbance at 652 nm at the beginning.)

Enzyme kinetics study: By monitoring the generation catalytic products using a UV-vis spectrophotometer and a kinetic method, we determined that the enzymatic reaction processes for the native enzymes and silver enzyme nanogel comply with the Michaelis–Menten equation:

$$Vo = \frac{\mathrm{V}_{max}[S]}{K_m + [S]}$$

where [S] is the substrate concentration, V_0 is the initial rate of product generation, and V_{max} is the maximum reaction rate. The Michaelis constant K_m represents the substrate concentration at which the reaction rate is half V_{max}. A lower K_m value indicates a stronger binding affinity between the enzyme and its substrate. The turnover number K_{cat} is defined as V_{max} /[E], where [E] is the enzyme concentration. Using the Lineweaver–Burk plot, we can express the equation as:

$$\frac{1}{V_0} = \frac{K_m}{k_{cat}\,[E][S]} + \frac{1}{k_{cat}[E]}$$

From this plot, both K_m and k_{cat} can be determined.

The GOX activity test of native GOX and Ag-nGOX was conducted as follows: the oxidation reaction of glucose was used to assess the GOX activity. In the presence of HRP and TMB, the generated H_2O_2, the oxidized products of oxTMB was monitored at 652 nm using a kinetic method. By varying the glucose concentration from 0.5 mM to 5 mM, the kinetics process was found to follow the Michaelis–Menten equation.

The HRP activity test of native HRP and Ag-nHRP was conducted as follows: The generation of oxidized TMB products was monitored at 652 nm using a kinetic method. By varying the H_2O_2 concentration from 0.5 mM to 5 mM while maintaining a constant TMB concentration, it was found that the TMB oxidation process catalyzed by HRP and Ag-nHRP follows the Michaelis–Menten equation. From the Lineweaver–Burk plot, significant kinetic parameters can be obtained.

The CAT activity test of native CAT and Ag-nCAT was conducted as follows: The decomposition of H_2O_2 was monitored at 240 nm using a kinetic method. By varying the H_2O_2 concentration from 2 mM to 12.5 mM, the kinetics process catalyzed by CAT and Ag-nCAT follows the Michaelis–Menten equation. From the Lineweaver–Burk plot, significant kinetic parameters can be obtained.

Evaluation of enzyme stability in vitro: The stability test was evaluated using the TMB oxidation test as described above. Specifically, 0Ag-nGHC and natural enzymes GHC (0.5 μg mL^{-1}) were incubated with HEPES (50 mM) solution of different pH values or incubated in the

water bath of elevated temperatures for 30 min to test enzymatic stability under various pH and temperature. Relative activity was calculated based on the catalytic reaction rates and the relative activity of enzymes in DI water at room temperature was set at 100% for comparison. For the long-term stability test, Ag-nGHC and natural enzymes were incubated with 25 mM HEPES at pH = 6.5 under room temperature for 7 days, the enzymatic stability was detected by UV-Vis every two days. The solvent stability tests of enzymes were carried out in the presence of i) trypsin (1 mg mL^{-1}) and ii) EDTA(0.5 wt%) after 30 min incubation at room temperature.

Measurement of pH value: Different groups (Control, Ag-nGOX, Ag-nHRP, Ag-nCAT, Ag-nGHC) were placed in a 37 °C water bath and pH values were measured by pH meter at different time points with glucose (5 mg mL^{-1}). The concentration of Ag-nGOX, Ag-nHRP, Ag-nCAT and Ag-nGHC applied in the experiment was 3 μg mL^{-1}.

Determination of dissolved oxygen (DO): The reaction activity of CAT in the system was verified by its ability to decompose H_2O_2 and generate oxygen. Each experimental group was incubated with H_2O_2 (1%) and its dissolved oxygen content was measured by an oxygen meter at different time points.

Cell culture: Mouse fibroblast L929 cells, obtained from ATCC, were cultured in Dulbecco's Modified Eagle Medium (DMEM) supplemented with 10% fetal bovine serum (FBS) and 1% penicillin-streptomycin. For sugar-free experiments, cells were incubated in glucose-free DMEM. All cultures were incubated at 37°C in a humidified atmosphere containing 5% CO_2.

Cytotoxicity assay: L929 cells were seeded at an initial density of 1.0×10^4 cells/well in 96-well plates and incubated overnight to facilitate cell adhesion. Subsequently, cells were exposed to varying concentrations of Ag-nGOX, Ag-nHRP, Ag-nCAT, and Ag-nGHC composites for 24 hours. Post-incubation, cells were treated with MTT reagent dissolved in the medium for 4 hours. The supernatant was then removed, and the formazan crystals were dissolved in DMSO. Absorbance at 560 nm was measured using a CMAX PLUS spectrophotometer (Molecular Devices, USA) to assess cell viability.

Evaluation of ROS clearance: L929 cells (5×10^4 cells/well) were plated in 48-well plates and incubated overnight for cell adherence. Post-adherence, cells were treated with serum-free DMEM containing H_2O_2 (100 μM) and then Ag-nGOX, Ag-nHRP, Ag-nCAT, or Ag-nGHC complexes (3 μg/mL-1) was added. After 24 hours, cells were incubated with DCFH-DA (10

μM) for 20 minutes. Fluorescence signals were determined by using an inverted fluorescence microscope (Dmi8, Leica, Germany) and quantified with ImageJ software.

O_2 assessment: After overnight incubation in 48-well plates, L929 cells were treated with serum-free DMEM containing 100 μM H_2O_2 for 6 hours, followed by another 6-hour incubation with different composites. Cells were then incubated with $[Ru(dpp)_3]$ Cl_2 probe (10 μg mL^{-1}) for 12 hours, washed with PBS for three times and analyzed for fluorescence signals using the Dmi8 microscope and ImageJ software.

In vitro antibacterial activity: The antibacterial efficacy against gram-negative Escherichia coli and gram-positive Staphylococcus aureus was assessed. A bacterial-contained suspension (100 μL, 10^7 CFU mL^{-1}) was resuspended in sterile Luria-Bertani (LB) medium (5 mL), supplemented with glucose (5 mg mL^{-1}) and composites (3 μg mL^{-1}). Cultures were incubated at 220 rpm, 37°C, and UV absorption at 600 nm was measured using an ELISA reader at different periods. Additionally, a sample from 24-hour cultures (100 μL) was plated on LB agar to examine bacterial growth.

Bacterial activity/toxicity test: A NucGreen/EthD-III double stain kit was employed to distinguish the living and death of bacteria. 1 volume of component A NucGreen and 2 volumes of component B EthD-III were mingled in a microcentrifuge tube. After the full mixture, 8 volumes of NaCl solution (0.85%) were appended to acquire 100× stain solution. 100× stain solution (1 μL) was added to bacterial suspension (100 μL) and every mixing well was cultured at room temperature under dark conditions for 15 min. The stained bacterial suspension drops (5 μL) were observed under a fluorescence microscope in which living bacteria had green or yellow-green fluorescence while dead bacteria had red fluorescence.

Macrophage transformation: Mouse mononuclear macrophage RAW264.7 cells (1×10^5 cells/well) were seeded in 6-well plates and stimulated with LPS (40 ng mL^{-1}) to induce M1 polarization. After removing the supernatant and washing three times, cells were incubated with composites (3 μg mL^{-1}) for 24 hours. Post-treatment, cells were suspended in PBS (0.5 mL) and stained with CD86 and CD206 antibodies for 30 minutes in the dark at room temperature. Following centrifugation, cells were resuspended in PBS and analyzed using flow cytometry (minimum 10,000 cells/sample). TNF-α, IL-10, and IL-1β levels in the supernatant were quantified using an ELISA kit.[64]

Immunofluorescence of phenotypic analysis of macrophages: RAW264.7 cells were used to evaluate the functions of silver-enzyme nanogels on phenotypic changes in macrophages. The cells (1×10^4 cells/well) were planted into 48-well plates with slides overnight and the cells were completely attached to the wall and incubated with the different silver-enzyme nanogels (3 μg/mL, FBS-DMEM-free). After 12 h, the cells were incubated with M1 marker FITC-CD86 antibody (1:100) (E_x=493 nm, E_m=522 nm) and antibody to M2 marker PE-CD206 (1:100) (E_x=588 nm, E_m=604 nm) overnight at 4°C. After that, it was rinsed 3 times with PBS to eliminate the staining solution and then immobilized with paraformaldehyde (4%). Finally, DAPI was unutilized to dye and seal the flakelets. High-sensitivity confocal laser microscope Zeiss LSM5 was employed to detect the images.

Diabetes rat model establishment: Sprague-Dawley (SD) rats (180-220 g) were acquired from Xiamen University's Experimental Animal Center and experiments were approved by the university's Animal Management and Ethics Committee (XMULAC20210054). To establish Type 1 diabetes models, rats were intraperitoneally injected with streptozotocin (STZ) dissolved in sterile citrate buffer (pH 4.2-4.5) at 70 μg kg^{-1}. Blood glucose levels were measured after two days; rats with blood glucose levels >16.7 mM were selected, while others received additional STZ injections. Rats maintained diabetic status during the whole wound healing process.

Chronic wound establishment, infection, and healing: Diabetic rats were infected with S. aureus and used for chronic wound healing assessment. After anesthetizing with chloral hydrate (10%, 3 mL kg^{-1}) and hair removal, 2 full-thickness skin wounds (9 mm×9 mm) were created on the back of each rat. Wounds were inoculated with S.aureus (50 μL, 10^8 CFU mL^{-1}) and rats were randomly divided into five different treated groups (for each group, n = 3), treated every two days, and monitored for weight and blood glucose. Anesthesia was performed with isoflurane, and wound healing was tracked using digital photography and calipers after 0, 2, 6, 10 and 14 days of treatment, evaluated using ImageJ software. The metal ring (Diameter: 1.5 cm) was used to standardize wound measurement in our experiments. It ensures that the images of the wounds are taken at a consistent magnification, preventing errors in calculating wound size. Wound area contracation ratio was calculated as

$$Wound\ size\ contraction\ ratio(\%) = \frac{Initial\ wound\ area - Wound\ area\ on\ a\ given\ day}{Initial\ wound\ area} \times\ 100\ \%$$

On day 14, all rats were sacrificed with tissue and organ extraction for further analysis.

Histological analysis: Collected tissues (skin, heart, liver, spleen, lung, kidney) were soaked in sucrose solutions (15% and 30%) for 24 and 12 hours, respectively. All the tissue sections (thickness: 8 μm) were prepared using a CM1900 cryostat (Leica, Germany) and stained with hematoxylin & eosin (H&E) for microscopic observation and analysis.

Immunofluorescence staining: After dehydration, all skin tissue samples were further prepared as frozen sections for fluorescence immunostaining. Skin tissue samples were fixed in paraformaldehyde (4%) for 30 min, followed by washing in PBS buffer. Then, the samples were blocked with 5% BSA, and stained with PE anti-mouse CD31 antibody and DHE at 4°C for 12 hours. Afterward, slides were stained with DAPI and imaged using an inverted fluorescence microscope. Fluorescence intensity was quantified using ImageJ software.

Statistical analysis: Experimental data were analyzed using Origin 2021b, expressed as mean ± SD of each set of triplicate samples, and differences were assessed using one way-ANOVA. Statistical differences were defined as $*p < 0.05$, $**p < 0.01$, and $***p < 0.001$.

Supporting Information

Supporting Information is available from the Wiley Online Library or from the author.

Acknowledgments

Y.M, X.L. and X.L contributed equally to this work. The authors would like to thank the National University of Singapore for the provision of a Ph.D. scholarship to Ms Ma Yedong. The authors would like to thank the support from the National Key R&D Program of China (Grant No. 2020YFA0908100), and the National Natural Science Foundation of China (82372119 and 82173750). X.F. and Z.L. would like to thank the financial support from the Agency for Science, Technology, and Research (A*STAR), Science and Engineering Research Council (SERC) Central Research Fund (Use-Inspired Basic Research) for this work. All animal research was conducted in accordance with the Guidelines for Care and Use of Laboratory Animals of Xiamen University and approved by the Animal Ethics Committee of Xiamen University.

Conflicts of interest

The authors declare that they have no known competing financial interests or personal relationships that could have appeared to influence the work reported in this paper.

Data Availability Statement

Research data are not shared.

Reference

[1] A. J. Boulton, L. Vileikyte, G. Ragnarson-Tennvall, J. Apelqvist, *The Lancet* **2005**, *366*, 1719.

[2] L. S. Geiss, Y. Li, I. Hora, A. Albright, D. Rolka, E. W. Gregg, *Diabetes Care* **2019**, *42*, 50.

[3] J. Huang, R. Yang, J. Jiao, Z. Li, P. Wang, Y. Liu, S. Li, C. Chen, Z. Li, G. Qu, K. Chen, X. Wu, B. Chi, J. Ren, *Nat. Commun.* **2023**, *14*, 7856.

[4] M. Brownlee, *Nature* **2001**, *414*, 813.

[5] Y. Chen, X. Wang, S. Tao, Q. Wang, P.-Q. Ma, Z.-B. Li, Y.-L. Wu, D.-W. Li, *Mil. Med. Res.* **2023**, *10*, 37.

[6] J. A. Bauer, M. Zámocká, J. Majtán, V. Bauerová-Hlinková, *Biomolecules* **2022**, *12*, 472.

[7] S. B. Bankar, M. V. Bule, R. S. Singhal, L. Ananthanarayan, *Biotechnol. Adv.* **2009**, *27*, 489.

[8] Y. Pang, H. Wang, Y. Yao, D. Chen, R. Yang, Z. Wang, J. Yang, Y. Li, W. Liu, *Adv. Funct. Mater.* **2023**, *33*, 2303095.

[9] L. Wang, G. Chen, L. Fan, H. Chen, Y. Zhao, L. Lu, L. Shang, *Adv. Sci.* **2023**, *10*, 2206900.

[10] M. Deng, M. Zhang, R. Huang, H. Li, W. Lv, X. Lin, R. Huang, Y. Wang, *Biomaterials* **2022**, *289*, 121790.

[11] F. Yang, R. Shu, B. Li, W. Dai, W. Chen, J. Sun, D. Bai, W. Yang, Y. Deng, *Chem. Eng. J.* **2024**, *482*, 149014.

[12] F. Huang, X. Lu, Y. Yang, Y. Yang, Y. Li, L. Kuai, B. Li, H. Dong, J. Shi, *Adv. Sci.* **2023**, *10*, 2203308.

[13] H. Xia, Z. Dong, Q. Tang, R. Ding, Y. Bai, K. Zhou, L. Wu, L. Hao, Y. He, J. Yang, H. Mao, Z. Gu, *Adv. Funct. Mater.* **2023**, *33*, 2215116.

[14] Q. Wang, Z. Luo, Y.-L. Wu, Z. Li, *Adv. NanoBiomed Res.* **2023**, *3*, 2200110.

[15] E. T. Hwang, S. Lee, *ACS Catal.* **2019**, *9*, 4402.

[16] L. Yu, Y. Sun, Y. Niu, P. Zhang, J. Hu, Z. Chen, G. Zhang, Y. Xu, *Adv. Healthc. Mater.* **2023**, *12*, 2202596.

[17] X. Zhang, Z. Wang, H. Jiang, H. Zeng, N. An, B. Liu, L. Sun, Z. Fan, *Sci. Adv.* **2023**, *9*, eadh1415.

[18] J. Yu, Y. Li, A. Yan, Y. Gao, F. Xiao, Z. Xu, J. Xu, S. Yu, J. Liu, H. Sun, *Adv. Sci.* **2023**, *10*, 2301919.

[19] Z. Li, X. Fan, Z. Luo, X. J. Loh, Y. Ma, E. Ye, Y.-L. Wu, C. He, Z. Li, *Nanoscale* **2022**, *14*, 14970.

[20] Y. Zheng, Z. Li, C. Liu, X. Fan, Z. Luo, Z. Li, Y.-L. Wu, *Front. Bioeng. Biotechnol.* **2023**, *11*, 1194398.

[21] Q. Li, M. Dong, Q. Han, Y. Zhang, D. Yang, D. Wei, Y. Yang, *J. Controlled Release* **2024**, *365*, 905.

[22] Y. Li, R. Fu, Z. Duan, C. Zhu, D. Fan, *Adv. Healthc. Mater.* **2022**, *11*, 2101849.

[23] P. Wang, L. Peng, J. Lin, Y. Li, Q. Luo, S. Jiang, H. Tian, Y. Zhang, X. Liu, J. Liu, *Chem. Eng. J.* **2021**, *415*, 128901.

[24] Y. Li, R. Fu, Z. Duan, C. Zhu, D. Fan, *Small* **2022**, *18*, 2200165.

[25] X. Yu, X. Fu, J. Yang, L. Chen, F. Leng, Z. Yang, C. Yu, *Mater. Today Bio* **2022**, *15*, 100308.

[26] Z. Luo, S. Jiang, Y.-L. Wu, Z. Li, *Ther. Deliv.* **2023**, *14*, 179.

[27] H. Lück, In *Methods of Enzymatic Analysis* (Ed.: Bergmeyer, H.-U.), Academic Press, **1965**, pp. 885–894.

[28] Y. Yu, R. Lin, H. Yu, M. Liu, E. Xing, W. Wang, F. Zhang, D. Zhao, X. Li, *Nat. Commun.* **2023**, *14*, 4249.

[29] L. Dai, M. Yao, Z. Fu, X. Li, X. Zheng, S. Meng, Z. Yuan, K. Cai, H. Yang, Y. Zhao, *Nat. Commun.* **2022**, *13*, 2688.

[30] Z. Zhao, J. Yan, K. Ling, R. Shi, R. Lv, B. Nie, J. Liu, *Adv. Funct. Mater.* **2021**, *31*, 2106471.

[31] M. Wu, Q. Wang, S. Chen, Z. Zhou, J. Li, H. Sun, J. Liu, G. Wang, F. Zhou, M. Sun, *J. Controlled Release* **2022**, *350*, 1.

[32] C. Liu, T. Wan, H. Wang, S. Zhang, Y. Ping, Y. Cheng, *Sci. Adv.* **2019**, *5*, eaaw8922.

[33] Y. Xiao, P. Chen, S. Lei, F. Bai, L. Fu, J. Lin, P. Huang, *Angew. Chem. Int. Ed.* **2022**, *61*, e202204584.

[34] C. Zheng, Q. Wang, Y. Wang, X. Zhao, K. Gao, Q. Liu, Y. Zhao, Z. Zhang, Y. Zheng, J. Cao, H. Chen, L. Shi, C. Kang, Y. Liu, Y. Lu, *Adv. Mater.* **2019**, *31*, 1902542.

[35] M. Yan, J. Du, Z. Gu, M. Liang, Y. Hu, W. Zhang, S. Priceman, L. Wu, Z. H. Zhou, Z. Liu, T. Segura, Y. Tang, Y. Lu, *Nat. Nanotechnol.* **2010**, *5*, 48.

[36] X. Fan, J. Lim, Z. Li, T. Wang, L. Jiang, S. Liu, L. Zhou, C. He, *J. Mater. Chem. B* **2021**, *9*, 3509.

[37] A. Beloqui, A. Y. Kobitski, G. U. Nienhaus, G. Delaittre, *Chem. Sci.* **2018**, *9*, 1006.

[38] M. Yan, J. Ge, Z. Liu, P. Ouyang, *J. Am. Chem. Soc.* **2006**, *128*, 11008.

[39] A. Rodriguez-Abetxuko, M. C. Morant-Miñana, F. López-Gallego, L. Yate, A. Seifert, M. Knez, A. Beloqui, *Adv. Funct. Mater.* **2018**, *28*, 1803115.

[40] G. Chen, A. A. Abdeen, Y. Wang, P. K. Shahi, S. Robertson, R. Xie, M. Suzuki, B. R. Pattnaik, K. Saha, S. Gong, *Nat. Nanotechnol.* **2019**, *14*, 974.

[41] J. Wen, D. Wu, M. Qin, C. Liu, L. Wang, D. Xu, H. V. Vinters, Y. Liu, E. Kranz, X. Guan, G. Sun, X. Sun, Y. Lee, O. Martinez-Maza, D. Widney, Y. Lu, I. S. Y. Chen, M. Kamata, *Nat. Biomed. Eng.* **2019**, *3*, 706.

[42] R. Yan, J. Ren, J. Wen, Z. Cao, D. Wu, M. Qin, D. Xu, R. Castillo, F. Li, F. Wang, Z. Gan, C. Liu, P. Wei, Y. Lu, *Adv. Mater.* **2022**, *34*, 2105670.

[43] M. Zhao, A. Zhu, X. Zheng, X. Qian, S. Zhang, C. Wu, C. Yu, J. Zhang, J. Li, *Adv. Healthc. Mater.* **2023**, *12*, 2300118.

[44] W. Fang, Z. Chi, W. Li, X. Zhang, Q. Zhang, *J. Nanobiotechnology* **2019**, *17*, 66.

[45] A. P. Richter, J. S. Brown, B. Bharti, A. Wang, S. Gangwal, K. Houck, E. A. Cohen Hubal, V. N. Paunov, S. D. Stoyanov, O. D. Velev, *Nat. Nanotechnol.* **2015**, *10*, 817.

[46] Y. Zheng, X. Lai, H. Ipsen, J. N. Larsen, H. Løwenstein, I. Søndergaard, S. Jacobsen, *Spectroscopy* **2007**, *21*, 211.

[47] M. P. Naghshbandi, H. Moghimi, In *Methods in Enzymology*, Elsevier, **2020**, pp. 431–451.

[48] H. Kaşgöz, S. Özgümüş, M. Orbay, *Polymer* **2003**, *44*, 1785.

[49] S. Fan, Q. Tang, J. Wu, D. Hu, H. Sun, J. Lin, *J. Mater. Sci.* **2008**, *43*, 5898.

[50] A. G. Kuba, Y. Y. Smolin, M. Soroush, K. K. S. Lau, *Chem. Eng. Sci.* **2016**, *154*, 136.

[51] P. K. Dara, R. Mahadevan, P. A. Digita, S. Visnuvinayagam, L. R. G. Kumar, S. Mathew, C. N. Ravishankar, R. Anandan, *SN Appl. Sci.* **2020**, *2*, 665.

[52] X. Liu, W. Ding, Y. Wu, C. Zeng, Z. Luo, H. Fu, *Nanoscale* **2017**, *9*, 3986.

[53] E. T. Hwang, S. Lee, *ACS Catal.* **2019**, *9*, 4402.

[54] G. Zhou, M. Li, *Adv. Mater.* **2022**, *34*, 2200871.

[55] J. I. Kang, K. M. Park, *Biomaterials* **2023**, *293*, 121943.

[56] M. N. Morshed, N. Behary, J. Guan, V. A. Nierstrasz, *ACS Sustain. Chem. Eng.* **2021**, *9*, 8879.

[57] K. Liang, R. Ricco, C. M. Doherty, M. J. Styles, S. Bell, N. Kirby, S. Mudie, D. Haylock, A. J. Hill, C. J. Doonan, P. Falcaro, *Nat. Commun.* **2015**, *6*, 7240.

[58] X. Fan, Z. Luo, Y. Chen, J. C. C. Yeo, Z. Li, Y.-L. Wu, C. He, *Acta Biomater.* **2022**, *142*, 274.

[59] G. C. Gurtner, S. Werner, Y. Barrandon, M. T. Longaker, *Nature* **2008**, *453*, 314.

[60] M. Sharifiaghdam, E. Shaabani, R. Faridi-Majidi, S. C. De Smedt, K. Braeckmans, J. C. Fraire, *Mol. Ther.* **2022**, *30*, 2891.

[61] A. E. Louiselle, S. M. Niemiec, C. Zgheib, K. W. Liechty, *Transl. Res.* **2021**, *236*, 109.

[62] M. Qin, Z. Cao, J. Wen, Q. Yu, C. Liu, F. Wang, J. Zhang, F. Yang, Y. Li, G. Fishbein, S. Yan, B. Xu, Y. Hou, Z. Ning, K. Nie, N. Jiang, Z. Liu, J. Wu, Y. Yu, H. Li, H. Zheng, J. Li, W. Jin, S. Pang, S. Wang, J. Chen, Z. Gan, Z. He, Y. Lu, *Adv. Mater.* **2020**, *32*, 2004901.

[63] A. M. G. Paramás, J. A. G. Bárez, C. C. Marcos, R. J. García-Villanova, J. S. Sánchez, *Food Chem.* **2006**, *95*, 148.

[64] C. Zhu, L. Ke, X. Ao, Y. Chen, H. Cheng, H. Xin, X. Xu, X. Loh, Z. Li, H. Lyu, Q. Wang, D. Zhang, Y. Ping, C. Wu, Y. Wu, *Adv. Mater.* **2024**, *36*, 2310078.